HHS Public Access

Author manuscript

Phys Med Biol. Author manuscript; available in PMC 2019 January 11.

Published in final edited form as:

Phys Med Biol. ; 63(2): 025015. doi:10.1088/1361-6560/aaa20b.

Simultaneous tumor and surrogate motion tracking with dynamic MRI for radiation therapy planning

Seyoun Park[1], **Rana Farah**[1], **Steven M. Shea**[2], **Erik Tryggestad**[3], **Russell Hales**[1], and **Junghoon Lee**[1]

[1]Department of Radiation Oncology and Molecular Radiation Sciences, Johns Hopkins University, Baltimore, MD, USA

[2]Department of Radiology, Stritch School of Medicine, Loyola University Chicago, Maywood, IL, USA

[3]Department of Radiation Oncology, Mayo Clinic, Rochester, MN, USA

Abstract

Respiration-induced tumor motion is a major obstacle for achieving high-precision radiotherapy of cancers in the thoracic and abdominal regions. Surrogate-based estimation and tracking methods are commonly used in radiotherapy, but with limited understanding of quantified correlation to tumor motion. In this study, we propose a method to simultaneously track the lung tumor and external surrogates to evaluate their spatial correlation in a quantitative way using dynamic MRI, which allows real-time acquisition without ionizing radiation exposure. To capture the lung and whole tumor, four MRI-compatible fiducials are placed on the patient's chest and upper abdomen. Two different types of acquisitions are performed in the sagittal orientation including multi-slice 2D cine MRIs to reconstruct 4D-MRI and two-slice 2D cine MRIs to simultaneously track the tumor and fiducials. A phase-binned 4D-MRI is first reconstructed from multi-slice MR images using body area as a respiratory surrogate and groupwise registration. The 4D-MRI provides 3D template volumes for different breathing phases. 3D tumor position is calculated by 3D-2D template matching in which 3D tumor templates in the 4D-MRI reconstruction and the 2D cine MRIs from the two-slice tracking dataset are registered. 3D trajectories of the external surrogates are derived via matching a 3D geometrical model of the fiducials to their segmentations on the 2D cine MRIs. We tested our method on ten lung cancer patients. Using a correlation analysis, the 3D tumor trajectory demonstrates a noticeable phase mismatch and significant cycle-to-cycle motion variation, while the external surrogate was not sensitive enough to capture such variations. Additionally, there was significant phase mismatch between surrogate signals obtained from the fiducials at different locations.

Keywords

dynamic MRI; lung tumor motion; tumor tracking; fiducial tracking; radiotherapy

1. Introduction

Radiotherapy for thoracoabdominal sites, including the lung, liver, and pancreas, are affected by breathing motion. Such respiration-induced tumor motion is a major obstacle for

achieving high-precision dosimetry and radiotherapy. Motion variability in the lung, liver, and pancreas over longer durations consistent with radiotherapy treatments has been demonstrated in numerous studies (Ozhasoglu and Murphy 2002, Seppenwoolde *et al* 2002, Gierga *et al* 2004, Shirato *et al* 2004, von Siebenthal *et al* 2007b). Additional treatment margins are typically added to the clinical target volume (CTV) to adequately treat the target tumor considering the setup uncertainty and the patient motion, which causes toxicity to healthy tissues (ICRU 1993; ICRU 1999). Therefore, significant resources have been focused at developing pre-treatment and intra-treatment motion management methods over the last decade (Hanley *et al* 1999, Shirato *et al* 2000, Remouchamps *et al* 2003, Hashimoto *et al* 2005, Berbeco *et al* 2006, Gibbs 2006, Kupelian *et al* 2007, Cerviño *et al* 2011).

In the pre-treatment stage, computed tomography (CT) is the reference image modality for radiotherapy planning and dose computation. Accordingly, respiration-correlated CT or 4D-CT is considered an effective tool to characterize tumor and normal tissue motion during radiotherapy. 4D-CT has become the gold standard for radiotherapy treatment planning in the context of breathing motion, and a pre-treatment 4D-CT scan is typically obtained to approximate the internal target volume (ITV), which is the extended volume by motion and geometric uncertainty from the gross target volume (GTV), for radiotherapy planning. 4D-CT is an approximation, though, because it only samples a limited number of tidal volumes. The sampled tumor excursion is then assumed to represent tumor motion over the course of a treatment session. (ICRU 1993, 1999). Additionally, CT deposits additional radiation dose to the patient, thus hindering its extension into acquiring information over timescales consistent with a treatment session.

During treatment, common motion management strategies currently used in radiotherapy include respiration gating (Li *et al* 2006, Berbeco *et al* 2005a, 2005b), real-time tumor tracking (Shirato *et al* 2000), and breath-hold techniques (Mah *et al* 2000, Rosenzweig *et al* 2000, Wong *et al* 1999) where external or internal surrogates are typically used to derive the patient and tumor position. While these methods may yield an improved treatment with reduced margins, they have inherent limitations. Tracking techniques often expose patients to ionizing radiation and an invasive procedure may be necessary for internal surrogate marker placement (Ionascu *et al* 2007). In addition, anatomic motion due to breathing is significantly variable between breathing cycles, treatment fractions, individual patients, and tumor location, and the respiratory motion can exhibit non-periodic, irregular patterns (Korin *et al* 1992, Stevens *et al* 2001). However, surrogate-based motion management strategies are widely used in clinics despite limited understanding of their limitations. Furthermore, tracking using implanted markers (Ionascu et al 2007, Korreman et al 2008) carry sub-sampled spatial information of the tumor, which may not be enough to represent tumor shape, size or the relational position of the tumor location in the organ.

Compared to current pre-treatment and intra-treatment approaches, magnetic resonance imaging (MRI) is advantageous due to its capability of visualizing the target tumor in contextual anatomy with excellent soft tissue contrast. MRI poses minimal risk to patients because it delivers non-ionizing radiation, making it highly suitable for longer duration and repeated scans (Cerviño *et al* 2011, Paganelli *et al* 2015a). Recent advances in dynamic MR imaging technologies enable MRI-guided radiation therapy (Liu *et al* 2004, Plathow *et al*

2004, Cai *et al* 2008, Bjerre *et al* 2013), which may better characterize organ motion. Dynamic MRI can improve 4D radiation therapy by giving continuous, rather than sample based data on tumor motion throughout a prolonged period of respiratory movement, either during a single treatment session or over a course of radiation treatment.

There have been studies to track tumor motion with 2D cine MR images (Sheng *et al* 2007, Feng *et al* 2009, Bjerre *et al* 2013, Tryggestad *et al* 2013), and more recently to predict the tumor motion by dynamic MRI (Seregni *et al* 2016). However, only a few groups have analyzed the correlation between the tumor motion and surrogate using 2D dynamic MR imaging techniques (Koch *et al* 2004, Feng *et al* 2009). These studies suggest that tumor positioning based on surrogates should be used with caution and imply that dynamic MRI is an attractive solution to address breathing motion and tumor tracking obstacles in radiotherapy. In this study, we propose a novel method to simultaneously track the 3D position of the tumor and external surrogates with dynamic MRI, which allows us to evaluate the correlation between the tumor motion and external surrogate signal for radiation therapy.

2. Methods

To simultaneously track the 3D tumor and external fiducial motions, we acquired 2D multi-slice and two-slice sagittal cine MR images as shown in Figure 1, with a slice acquisition frequency of approximately 4 Hz on average. Four MRI-compatible fiducials were placed on the thorax and upper abdominal regions to provide external surrogate signals. The sagittal slice was preferred because the tumor and fiducial motions are occurring mainly along superior-inferior (SI) and anterior-posterior (AP) directions with much smaller lateral motion. Multi-slice 2D cine MR images were acquired in an interleaved fashion to avoid signal cross-talk between adjacent slices. The total number of slices was set to ensure coverage of the whole tumor, and was therefore variable between patients. This group of slices was then repeatedly acquired to fully sample the respiratory cycle. This data allowed us to retrospectively reconstruct a 4D-MRI volume that provides a representative depiction of one-cycle respiration motion, somewhat analogous to 4D-CT (von Siebenthal *et al* 2007a, Paganelli *et al* 2015b). However, this 4D-MRI cannot fully represent the tumor and fiducial motions over a long period of time. To simultaneously track the motions of both tumor and external fiducials, a two-slice 2D cine MR scan was performed; the reduced number of slices compared to the multi-slice technique provided the necessary temporal resolution to adequately sample breath-to-breath variations in the respiratory cycle. Two images were obtained at the fixed positions of π^R and π^L in an alternating and repetitive way as shown in Figure 1(c). In this scan, one slice was positioned to capture both the tumor and two fiducials located on the tumor side, while the other slice was positioned to capture the remaining two fiducials on the non-tumor side as shown in Figure 1(a).

2.1. 4D-MRI reconstruction and tumor template

4D-MRI volumes are reconstructed from the multi-slice MR images. 4D-MRI reconstruction was useful for obtaining not only representative volumes for one breathing cycle, but also 4D tumor templates. The obtained 4D tumor templates were later used to track the 3D tumor

motion from 2D MR images. Figure 2 describes our 4D-MRI reconstruction workflow. The patient's respiratory signal was extracted by computing body area on each 2D image (Liu *et al* 2014). Each respiration cycle was divided into N=10 breathing phases and the collected multi-slice MR images are sorted into these N breathing phases. Each phase bin contained multiple MR images that were roughly at similar breathing phase but with variations due to uncertainties in phase binning. To reconstruct a 2D image from multiple sorted images at each slice location and each bin, we performed groupwise registration between the sorted images (Farah *et al* 2015). Groupwise registration is a technique to mitigate uncertainties in multiple images (usually images in population) by incorporating them through registration process (Balci *et al* 2007, Yushkevich *et al* 2012). As shown in Figure 2(b), we performed groupwise registration between multiple sorted images to compute a 2D slice image at each slice location and bin. We repeated this process across different slice locations and breathing phases. The reconstructed slices per breathing phase were then slice-stacked to form a representative 4D image. The final outcome was a series of N=10 reconstructed volumes, $\Psi = (V_0, \ldots, V_{N-1})$ each of which represented a 3D volume at each breathing phase. Tumor volumes were segmented from the 4D-MRI reconstruction volumes by region-growing from user-selected points. The segmented tumors were served as the reference templates for 3D motion tracking in the next step.

2.2. Tumor tracking

3D tumor motion was determined from the two-slice cine MRI acquisition. We calculated the 3D motion from the 2D scan by 3D (tumor template volumes in 4D-MRI) to 2D (cine MRI) registration. Because the 2D tracking images and 4D-MRI are defined in the same MR coordinate system, their relative geometry is a known a *priori*. Given the 3D MRI volume V_i at the i^{th} phase, let us denote the segmented tumor volume as $R_i \subset V_i$ and the centroid of R_i as $\mathbf{c}_i$. To match the tumor region, the sequential 2D cine MR images $\pi_t^S(t=1, 2, \ldots, S \in [R, L])$ were sorted by the same phase-binning approach based on body area as used for 4D-MRI reconstruction. For each time stamp, t, a rigid transformation T_t between the 3D tumor template in the same phase and the target 2D image was estimated by 3D template to 2D image registration. We assume that there was no tumor shape change between the 3D template and the 2D slice image that were obtained at the same breathing phase. We maximized normalized cross-correlation (NCC) between the 2D slice image and cross-section of the 3D tumor template on the 2D slice image plane. To reduce computation time, NCC was computed only within a region-of-interest (ROI) expanded from R_i. Image intensity was used for NCC computation and we represented the tumor motion by the series of the transformed center locations $T_t(\mathbf{c}_i)$. The rigid transformation included six parameters, consisting of xyz-translation and Euler angles, and the optimal T_t which maximizes NCC was found by the quasi-Newton method(Press *et al* 2007). An example of tumor tracking is shown in Figure 3.

2.3. Fiducial tracking

The MRI-compatible fiducial designed for our study consists of four cylinders filled with 0.9% sodium chloride (normal saline) that were mounted on the top and bottom side of a V-shaped acrylic body with the bounding box size of 8.2×7.6×2.4 cm^3 (width × height ×

thickness). When imaged sagittally or quasi-sagittally, it produces a unique 2D slice cut as shown in Figure 4(d–e). The 3D motion of the fiducial is calculated by matching its 3D geometrical model to 2D cine images. A 3D geometrical model of the fiducial was derived from its CT scan where center lines of the four cylinders and centroid of the fiducial body were computed. In each 2D MR image, the four cylinders from each fiducial are clearly visible as bright ellipses. The fiducial ellipses were individually segmented and indexed in each of the two-slice MR images. The 3D location and orientation of the fiducial in the MRI coordinate frame is thus calculated by matching its 3D geometrical model to 2D cine images.

A line segment connecting the two end points $\mathbf{p}, \mathbf{q} \in \mathbb{R}^3$ can be written as $\mathbf{l}(t) = \mathbf{p}+(\mathbf{q}-\mathbf{p})t$ in parametric form with $t \in \mathbb{R}$ $(0 < t < 1)$. Since there are 4 cylinders in a fiducial, the fiducial geometry can be defined by an ordered set of four line segments $\mathbf{F} = (\mathbf{l}_1, \mathbf{l}_2, \mathbf{l}_3, \mathbf{l}_4)$. The fiducial features, as shown in Figure 4(d), were segmented by thresholding and morphological filtering and subsequently indexed by their locations. Fiducial tracking was then realized by a rigid registration, determined by fitting the CT-based fiducial model **F** to its MR segmentation. Formally, the image plane is defined as $\mathbf{n}\cdot(\mathbf{x}-\mathbf{o}) = 0$, where **o** is the origin of the plane and **n** is the plane normal vector. The intersection point **x** between the line segment and the plane can be computed by

$$\mathbf{x}=\mathbf{p}+\frac{\mathbf{n}\cdot(\mathbf{o}-\mathbf{p})}{\mathbf{n}\cdot\mathbf{d}}\mathbf{d}=\frac{(\mathbf{n}\cdot\mathbf{o})\mathbf{d}+\mathbf{n}\times(\mathbf{p}\times\mathbf{d})}{\mathbf{n}\cdot\mathbf{d}} \quad (1)$$

where $\mathbf{d} = (\mathbf{q}-\mathbf{p})/\left\|\mathbf{q}-\mathbf{p}\right\|$. Let $T(\mathbf{x})$: $\mathbb{R}^3 \rightarrow \mathbb{R}^3$ the rigid transformation of the line segment to the image plane. To estimate the 3D center of the fiducial markers from the 2D MR images, we find the optimal transformation which minimizes the following cost function

$$E=\sum_{i=1}^{4}\|\mathbf{c}_i - T(\mathbf{x}_i)\|^2 \quad (2)$$

where $\mathbf{c}_i$ is the center of the segmented marker in 2D MRI as shown in Figure 4(e) and $T(\mathbf{x})$ is computed as

$$T(\mathbf{x})=\frac{(\mathbf{n}\cdot\mathbf{o})T(\mathbf{d})+\mathbf{n}\times(T(\mathbf{p})\times T(\mathbf{d}))}{\mathbf{n}\cdot T(\mathbf{d})} \quad (3)$$

The rigid transformation T has six degrees of freedom in this model ([*x*, *y*, *z*] translation and Euler angles). To find an optimal solution of this non-linear least squares problem of (2), we used the well-known Levenberg-Marquardt algorithm (Press *et al* 2007), and the initial solution was estimated from the trapezoidal geometry of the fiducial image in 2D MR images. Finally, the fiducial centroid trajectory of each fiducial was computed based on the estimated transformation, yielding a surrogate signal.

2.4. Simulations

To evaluate the accuracy of the proposed dynamic MRI-based tumor tracking, we simulated 2D dynamic MR image acquisition process using 4D-MR images reconstructed from our multi-slice MR scan. We then applied our tumor tracking algorithm to the simulated 2D dynamic MR images. This simulation study is useful as we know the 3D ground truth position of the tumor at the time of 2D MRI acquisition, therefore can quantitatively assess the accuracy of our tracking. To estimate and simulate the lung and tumor motions during breathing, we first segmented only lung region $\mathbf{L}_i \subset \mathbb{R}^3$ (i=0, …, n−1) from each phase volume. We registered all 10 lung regions (equivalent to 10 breathing phases) in the 4D-MRI and performed principal components analysis (PCA) on the computed deformation fields. We used the 50% phase as the reference, $\hat{\mathbf{L}}$, and deformably registered the other phases $\mathbf{L}_j$ (j=1, …, n−1, $\mathbf{L}_j \neq \hat{\mathbf{L}}$) to $\hat{\mathbf{L}}$ using the demons registration method (Park *et al* 2017). Deformation vector fields $\mathbf{d}_j$ were obtained for each registration between $\mathbf{L}_j$ and $\hat{\mathbf{L}}$ from which the breathing cycle can be represented as $\mathbf{L}=\hat{\mathbf{L}}+\sum_{j=1}^{n-1} w_j \mathbf{d}_j$ To simulate virtual respiration volume, we extracted principal modes of variation of the deformation. From the matrix $\mathbf{D} = [\mathbf{d}_1 \cdots \mathbf{d}_{n-1}]$, principal components of the deformation can be computed by singular vector decomposition (SVD) as shown

$$\mathbf{D}=\sum_{i=1}^{r} \lambda_i \cdot \mathbf{u}_i \cdot \mathbf{v}_i{}^T \quad (4)$$

where r (< n) is the rank of $\mathbf{D}$, $\{\lambda_i\}$ are non-negative and eigenvalues in decreasing order, $\{\mathbf{u}_i\}$ are corresponding eigenvectors in space domain, and $\{\mathbf{v}_i\}$ are eigenvectors in temporal domain. By selecting K ($K \ll$ r) eigenvectors from $\{\mathbf{u}_i\}$ and associated weights $w_k(t)$, we can calculate the 3D spatial transformation for each voxel based on a small set of major modes of variation

$$\mathbf{L}(t) \approx \hat{\mathbf{L}}+\sum_{k=1}^{K} \mathbf{u}_k w_k(t) \quad (5)$$

3. Experiments and Results

We tested our method on 10 lung cancer patients under an IRB (Institutional Review Board) approved protocol. MR images were acquired using Siemens Magnetom Espree 1.5T scanner (Siemens Medical Solutions, Malvern, PA) with a balanced steady-state free precession sequence (TrueFISP, TR≈3 ms, TE=1.22 ms, flip angle=77–79°). Multi-slice MR images for 4D-MRI reconstruction were first acquired; subsequently, two-slice cine MRI for tracking was acquired. The patient breathed normally during both scans. Acquired images were corrected for geometric distortion using the Siemens distortion correction function provided within Syngo platform (Siemens AG, Erlangen, Germany). The obtained 2D MR images had a spatial resolution of 2×2 mm^2 with slice thickness and spacing of 5 mm. The slice acquisition frequency was approximately 4 Hz. The number of slices in the multi-slice MR scan varied between 10 and 15 depending on the tumor size. Five minutes of multi-slice

and each two-slice MR image acquisition were used to derive the 4D-MRI in this study. Therefore, at each slice location, about 600 MR images were acquired for two-slice scan, and 80-120 images were acquired for multi-slice scan depending on the tumor size. Given that we sorted multi-slice MR images into 10 breathing phases, there were approximately 8-12 images obtained at each breathing phase and slice location.

We tracked motions of the target tumor and 4 fiducial markers (i.e., surrogate signals) using the two-slice 2D MR images. We analyzed the correlation between the tumor and each fiducial motion, and also assessed the sensitivity of 4D-CT-driven ITV using the estimated tumor motion. 4D-CT images of 10 phases for each patient were obtained by Philips Brilliance Big Bore scanner (Philips Medical Systems, Cleveland, OH, USA) with spatial resolutions of [0.98, 1.27]×[0.98, 1.27] mm^2 and 3mm slice thickness.

3.1. Evaluation by simulation

Based on (5), we generated 4D motion of randomly selected five cases among total 10 cases. The overall target registration errors (TREs) of the deformable image registration showed 2.38±1.03mm for the whole five cases with 30 feature points from each case. To account for irregularity in real patient's breathing, we added random noise to $w_k(t)$ with Gaussian distribution $N(0, 0.05\sigma_k)$, where σ_k is the standard deviation of k^{th} eigenvector. A series of 2D slice images were obtained by cutting $\mathbf{L}(t)$ at the same slice location with the same frequency as our 2D MR image acquisition. The same tumor tracking process described in Section 2.2 was performed to the simulated 2D slice images. Note that the ground truth tumor location was known for each simulated 2D slice image; therefore, the tumor tracking accuracy was computed by measuring the Euclidean distance between the estimated tumor centroid and the ground truth.

In our experiments, K=2 in (5) was selected because more than 90% of lung motion could be described by the first two eigenvectors, which is consistent with other studies (Li *et al* 2011, Stemkens *et al* 2016). Figure 5 shows the plot of normalized eigenvalues for two test cases.

Table 1 shows the tumor tracking errors for 5 simulation cases. Since the rotational tracking error was very small compared with the translation error for all 5 cases, here we report errors in tumor centroid tracking in Table 1. The overall mean error in 3D shows 1.63 mm (< 2mm) with 2×2×5mm resolution MR slice, which is acceptable to analyze the successive patient data. The major errors are from right-left (RL) direction in most cases, which is reasonable considering only sagittal planes are acquired in our experiments. During the registration iteration, 3D tumor template volume keeps being resampled based on the currently estimated transformation along the 2D image plane, from which sub-voxel registration accuracy can be achieved (Tian and Huhns 1986, Debella-gilo and Kääb 2011, Karybali *et al* 2008). The 3D-2D registration handles not only the in-plane alignment but also out-of-plane alignment altogether.

3.2. In-vivo experiments

3.2.1. Tumor vs surrogate motion—Since external fiducial and tracking systems are used to extract breathing signal in clinical practice, we extracted a 3D surrogate motion

signal from the largest motion direction of each fiducial while tumor motion was analyzed by breaking into the three orthogonal directions (AP, SI, RL). Figure 6 shows two examples of the tumor motion and surrogate signal comparison under normal breathing. In general, the surrogate signal correlated well with the tumor motion, but often showed significant phase mismatch.

Cross-correlation (CC) between each fiducial and the tumor motion signals is described in Table 2. Overall CC values for the ten cases showed 16.60±7.55, 14.14±8.20, and 8.75±3.00 for SI, AP, and RL directions, respectively. Note that cross-correlation is a global comparison of two signals for the whole scanning time and therefore does not show the local mismatch. In addition, there is significant amplitude variation in the tracking signals of the tumor and fiducials, which makes a proper interpretation of the presented values hard. To better measure the local phase mismatch, we also measured the mean and standard deviations of phase differences between the tumor and fiducial motion signals (also shown in Table 2). To compute the phase differences, we identified all the peaks in both tumor motion and fiducial signals, and computed time differences between the matched peaks.

Figure 7 summarize the phase differences in each direction as a box plot which visualizes the range of mean phase differences between 4 fiducial markers.

3.2.2. Tumor motion vs ITV—We compared the tracked tumor motion with the standard 4D-CT-based estimate of ITV by first rigidly registering the 4D-CT volumes to 4D-MR volumes. We used the spine and posterior lung boundary as the landmarks since the patient was scanned in the supine position for both CT and MRI, and was also treated in this position. We assessed the sensitivity of the CT-based ITV by computing the percentage of time the MR-estimated tumor volume was contained within the CT-ITV over the course of the 5 minute MR-tracking scan. We also computed the volume percentage within the ITV corresponded to normal tissues on average during the 5-minute scan and the results are described in Table 3. On average, the tumor volumes were within ITV for 85.1% (81.6-89.1%), and 44.8% (38.2-53.1%) of ITV corresponded to normal tissues. These results imply that the 4D-CT-driven ITV may not accurately represent the actual long-duration tumor motion occurring during a radiation treatment session, which has been shown by other studies (Minn *et al* 2009).

Considering that the planning target volume (PTV) is determined by adding a margin to ITV, we performed the same comparison of the tracked tumor motion to PTV. While PTV covered the tumor motions well for all cases, on average 67.12 ± 8.7 % of PTV D95 corresponded to normal tissues, implying that a significant portion of normal tissues received unnecessary radiation exposure.

4. Discussion

As shown in Figure 6 and 7, the phase mismatch was often systematic, but there existed significant transient phase mismatches, which may pose significant problems in external surrogate-based tumor motion tracking during radiotherapy. We also observed significant phase difference between the upper (placed to the upper chest) and lower (placed to the

lower chest close to abdomen) fiducials. This is due to the variation of the patient's surface motion around the upper and lower chest areas depending on breathing patterns. This suggests that the position of the external fiducial should be carefully chosen and the tumor location also has to be considered when estimating its motion based on the surrogate signal. This gives the observations from our experiments that the differences in tumor and surrogate motion signals along SI direction were small in general as shown in (Ionascu *et al* 2007), but not for all ten cases, and also different signal correlation patterns were observed depending on the fiducial locations as shown in Table 2 and Figure 7.

Compared with internal/external marker-based approaches (Ionascu *et al* 2007, Korreman *et al* 2008), our image-driven motion management has advantage to provide more quantitative information about ITV coverage. In our 4D-CT based ITV comparison, on average 15% of tumor region was not covered by CT-based ITV and corresponding normal tissues were included into ITV. Although 4D-CT-driven PTV covered tumor motion for all 10 cases examined in this study, over 65% of PTV corresponded to normal tissues. This implies that the proposed 4D-MRI-based tumor motion tracking method can be a very useful tool to analyze the tumor motion for long duration that is equivalent to the fractionated radiation therapy and adjust the treatment margin. Taken together, these data suggest that the surrogate-based tumor motion estimation may have significant amount of uncertainties to manage the tumor motion during radiotherapy. Based on the proposed framework, additional quantitative analysis such as tracking error or correlation according to the tumor location and size is possible with larger cohort of patients.

There are several prior studies which tracked 3D tumor motion using orthogonal, e.g., sagittal and coronal, 2D dynamic MRI (Bjerre *et al* 2013, Tryggestad *et al* 2013). In our study, we scanned the patient only at sagittal orientation to simultaneously track both tumor and 4 external fiducials. Since the external fiducials were placed in 4 different locations, it was not possible to capture the motions of the tumor and all 4 fiducials using an orthogonal scan protocol. Instead, we tracked their 3D motions from two sagittal scans using image processing techniques: 4D tumor template to 2D MR image matching for the tumor, and 3D model to 2D MR image matching for the fiducials. In this method, tumor tracking error in RL direction is likely to be larger than the other directions. However, major tumor motion occurs along SI and AP directions and the motion in RL direction is relatively smaller. As shown in our simulation study (Table 1), the proposed method showed reasonable accuracy in all three directions as well as in 3D with only slightly larger error in RL direction than the other directions. Additionally, one may concern that rigid 3D-2D registration may not be sufficient enough to account for potential tumor deformation. We observed that deformation of the tumor shape was negligible in all of our patients. Since our 3D tumor template is extracted from 4D-MRI volume reconstructed at the same breathing phase as the 2D tracking MR image, potential tumor deformation, although usually small, is already captured in our approach. The robustness of the tacking algorithm may be further improved if a breathing guide system is combined, e.g., audiovisual biofeedback (Lee *et al* 2016) which has proven to improve intra- and inter-fraction tumor motion consistency measured in MRI compared with free-breathing.

It is also important to note that there exist artifacts in 4D-MRI reconstruction due to retrospective image sorting. Most notable artifact of retrospective 4D-MRI reconstruction is inconsistent reconstruction along the through-plane direction, i.e., lateral direction in our case as our images were acquired at (semi)sagittal orientation. Such inconsistency may result in inconsistent 3D tumor template, leading to erroneous tumor tracking by the proposed 3D tumor template to 2D image registration. In order to minimize such inconsistency, our 4D-MRI reconstruction process takes multiple measured 2D images at each breathing phase and slice location, and performs groupwise registration of all sorted images, requiring high correlation between reconstructed slices. The groupwise registration finds a slice reconstruction that mitigates uncertainties and biases between the multiple measured images, therefore produces smoother reconstruction along the through-plane direction with higher signal to noise ratio compared to conventional averaging approaches. However, improved 4D-MRI reconstruction would further improve the tumor tracking accuracy of the proposed method.

Unlike the simulation, there could be large motion deviations in real patients caused by a significant breathing pattern change, gross patient motion, or coughing. Such a large deviation may result in images with missing tumor or fiducials (since tumor or fiducials could move out of plane). However, this motion is transient, and unobserved tumor or fiducial locations were interpolated using adjacent time frames.

In this study, our tracking was performed offline after the MRI scan. Tumor tracking for each time frame takes approximately 800ms in our current Matlab implementation. Although real-time tumor tracking is not the goal of this study, the computation time can be further reduced by incorporating a motion prediction algorithm (Verma *et al* 2011) into the tracking and optimizing the algorithm. Tracking with motion prediction may better cope with the missing data problem than simple interpolation. A robust and fast 3D tumor tracking algorithm based on 2D dynamic MRI will enable intrafractional tracking of target tumor when used with recently developed MR-LINAC's. Combined with motion adaptive planning and treatment approaches (Keall *et al* 2001, Niu *et al* 2017), it can allow for margin reduction in PTV with high tumor tracking accuracy.

5. Conclusions

We proposed a novel method to simultaneously track tumor and external fiducial motions with dynamic MRI, and quantitatively measured the correlation between the external surrogate signals and internal tumor motions. 4D-MRI reconstruction from multi-slice dynamic MRI scan allows us to build a 4D tumor template which is then used to track 3D tumor motion from 2D dynamic MR images by 3D(tumor template)-2D MR image registration. MR-compatible fiducials with a unique configuration enables 3D fiducial motion tracking from 2D MR images by model to 2D image matching. Using the proposed methods, we simultaneously tracked both tumor and 4 fiducials placed at different locations on the patient's chest. The tumor motion and surrogate signal correlated well in general, but often showed systemic and/or transient variations in phase. Additionally, the ITV derived from 4D-CT, which is a single snapshot of one breathing cycle, was not sensitive enough to capture the tumor motion for longer time durations. Although tested on a limited number of

patients, our results suggest that surrogate-based lung tumor motion management in radiation therapy should be used with caution. Furthermore, the proposed method showed its utility to enable patient-specific analysis of tumor motion that is monitored for long duration of time equivalent to the treatment, thus helping us determine the best motion management method at the time of radiotherapy planning.

Acknowledgments

This work was supported by NIH/NCI under the grant R21CA178455.

References

Balci SK, Goll P, Shenton M, Wells WM. Free-Form B-spline Deformation Model for Groupwise Registration. Med Image Comput Comput Assist Interv. 2007

Berbeco RI, Mostafavi H, Sharp GC, Jiang SB. Towards fluoroscopic respiratory gating for lung tumours without radiopaque markers. Phys Med Biol. 2005a

Berbeco RI, Nishioka S, Shirato H, Chen GTY, Jiang SB. Residual motion of lung tumours in gated radiotherapy with external respiratory surrogates. Phys Med Biol. 2005b

Berbeco RI, Nishioka S, Shirato H, Jiang SB. Residual motion of lung tumors in end-of-inhale respiratory gated radiotherapy based on external surrogates. Med Phys. 2006

Bjerre T, Crijns S, Rosenschöldaf PM, Aznar M, Specht L, Larsen R, Keall P. Three-dimensional MRI-linac intra-fraction guidance using multiple orthogonal cine-MRI planes. Phys Med Biol. 2013; 58:4943–50. Online: http://stacks.iop.org/0031-9155/58/i=14/a=4943?key=crossref.7167a3063e054239f9e41212d67c5144. [PubMed: 23807514]

Cai J, Read PW, Larner JM, Jones DR, Benedict SH, Sheng K. Reproducibility of interfraction lung motion probability distribution function using dynamic MRI: statistical analysis. Int J Radiat Oncol Biol Phys. 2008

Cerviño LI, Du J, Jiang SB. MRI-guided tumor tracking in lung cancer radiotherapy. Phys Med Biol. 2011

Debella-gilo M, Kääb A. Sub-Pixel Precision Image Matching for Displacement Measurement of Mass Movements Using Normalised Cross-Correlation. Remote Sens Environ. 2011; 115:181–6.

Farah R, Shea SM, Tryggestad E, Forbang RT, Wong J, Hales R, Lee J. 4D-MRI reconstruction using group-wise registration. AAPM Annual meeting. 2015

Feng M, Balter JM, Normolle D, Adusumilli S, Cao Y, Chenevert TL, Ben-Josef E. Characterization of Pancreatic Tumor Motion Using Cine MRI: Surrogates for Tumor Position Should Be Used With Caution. Int J Radiat Oncol Biol Phys. 2009

Gibbs IC. Frameless image-guided intracranial and extracranial radiosurgery using the Cyberknife robotic system. Cancer Radiother. 2006

Gierga DP, Chen GTY, Kung JH, Betke M, Lombardi J, Willett CG. Quantification of respiration-induced abdominal tumor motion and its impact on IMRT dose distributions. Int J Radiat Oncol Biol Phys. 2004

Hanley J, Debois MM, Mah D, Mageras GS, Raben A, Rosenzweig K, Mychalczak B, Schwartz LH, Gloeggler PJ, Lutz W, Ling CC, Leibel SA, Fuks Z, Kutcher GJ. Deep inspiration breath-hold technique for lung tumors: The potential value of target immobilization and reduced lung density in dose escalation. Int J Radiat Oncol Biol Phys. 1999

Hashimoto T, Shirato H, Kato M, Yamazaki K, Kurauchi N, Morikawa T, Shimizu S, Ahn YC, Akine Y, Miyasaka K. Real-time monitoring of a digestive tract marker to reduce adverse effects of moving organs at risk (OAR) in radiotherapy for thoracic and abdominal tumors. Int J Radiat Oncol Biol Phys. 2005

ICRU. Prescribing, Recording, and Reporting Photon Beam Therapy (Report 62). ICRU Rep. 1999

ICRU. Prescribing, recording and reporting photon beam therapy (ICRU report 50). ICRU Rep. 1993

Ionascu D, Jiang SB, Nishioka S, Shirato H, Berbeco RI. Internal-external correlation investigations of respiratory induced motion of lung tumors. Med Phys. 2007; 34:3893–903. [PubMed: 17985635]

Karybali IG, Psarakis EZ, Berberidis K, Evangelidis GD. An efficient spatial domain technique for subpixel image registration. Signal Process Image Commun. 2008; 23:711–24.

Keall PJ, Kini VR, Vedam SS, Mohan R. Motion adaptive x-ray therapy: A feasibility study. Phys Med Biol. 2001; 46:1–10. [PubMed: 11197664]

Koch N, Liu HH, Starkschall G, Jacobson M, Forster K, Liao Z, Komaki R, Stevens CW. Evaluation of internal lung motion for respiratory-gated radiotherapy using MRI: Part I - Correlating internal lung motion with skin fiducial motion. Int J Radiat Oncol Biol Phys. 2004

Korin HW, Ehman RL, Riederer SJ, Felmlee JP, Grimm RC. Respiratory kinematics of the upper abdominal organs: A quantitative study. Magn Reson Med. 1992

Korreman SS, Trine J-N, Boyer AL. Respiratory gated beam delivery cannot facilitate margin reduction, unless combined with respiratory correlated image guidance. Radiother Oncol. 2008; 86:61–8. [PubMed: 18039549]

Kupelian P, Willoughby T, Mahadevan A, Djemil T, Weinstein G, Jani S, Enke C, Solberg T, Flores N, Liu D, Beyer D, Levine L. Multi-institutional clinical experience with the Calypso System in localization and continuous, real-time monitoring of the prostate gland during external radiotherapy. Int J Radiat Oncol Biol Phys. 2007

Lee D, Greer PB, Ludbrook J, Arm J, Hunter P, Pollock S, Makhija K, O'Brien RT, Kim T, Keall P. Audiovisual Biofeedback Improves Cine-Magnetic Resonance Imaging Measured Lung Tumor Motion Consistency. Int J Radiat Oncol Biol Phys. 2016; 94:628–36. [PubMed: 26867892]

Li R, Lewis JH, Jia X, Zhao T, Liu W, Wuenschel S, Lamb J, Yang D, Low DA, Jiang S. On a PCA-based lung motion model. Phys Med Biol. 2011; 56:6009–30. [PubMed: 21865624]

Li XA, Stepaniak C, Gore E. Technical and dosimetric aspects of respiratory gating using a pressure-sensor motion monitoring system. Med Phys. 2006

Liu HH, Koch N, Starkschall G, Jacobson M, Forster K, Liao Z, Komaki R, Stevens CW. Evaluation of internal lung motion for respiratory-gated radiotherapy using MRI: Part II-margin reduction of internal target volume. Int J Radiat Oncol Biol Phys. 2004

Liu Y, Yin FF, Chang Z, Czito BG, Palta M, Bashir MR, Qin Y, Cai J. Investigation of sagittal image acquisition for 4D-MRI with body area as respiratory surrogate. Med Phys. 2014

Mah D, Hanley J, Rosenzweig KE, Yorke E, Braban L, Ling CC, Leibel SA, Mageras G. Technical aspects of the deep inspiration breath-hold technique in the treatment of thoracic cancer. Int J Radiat Oncol Biol Phys. 2000

Minn AY, Schellenberg D, Maxim P, Suh Y, McKenna S, Cox B, Dieterich S, Xing L, Graves E, Goodman Ka, Chang D, Koong AC. Pancreatic tumor motion on a single planning 4D-CT does not correlate with intrafraction tumor motion during treatment. Am J Clin Oncol. 2009

Niu Y, Betzel GT, Yang X, Gui M, Parke WC, Yi B, Yu CX. Planning 4D intensity-modulated arc therapy for tumor tracking with a multileaf collimator. Phys Med Biol. 2017; 62:1480–500. [PubMed: 28052050]

Ozhasoglu C, Murphy MJ. Issues in respiratory motion compensation during external-beam radiotherapy. Int J Radiat Oncol Biol Phys. 2002

Paganelli C, Seregni M, Fattori G, Summers P, Bellomi M, Baroni G, Riboldi M. Magnetic resonance imaging-guided versus surrogate-based motion tracking in liver radiation therapy: A prospective comparative study. Int J Radiat Oncol Biol Phys. 2015a

Paganelli C, Summers P, Bellomi M, Baroni G, Riboldi M. Liver 4DMRI: A retrospective image-based sorting method. Med Phys. 2015b; 42:4814–21. Online: http://www.ncbi.nlm.nih.gov/pubmed/26233208. [PubMed: 26233208]

Park S, Plishker W, Quon H, Wong J, Shekhar R, Lee J. Deformable registration of CT and cone-beam CT with local intensity matching. Phys Med Biol. 2017; 62:927–47. [PubMed: 28074785]

Plathow C, Ley S, Fink C, Puderbach M, Hosch W, Schmähl A, Debus J, Kauczor HU. Analysis of intrathoracic tumor mobility during whole breathing cycle by dynamic MRI. Int J Radiat Oncol Biol Phys. 2004

Press, W., Flannery, B., Teukolsky, S., Vetterling, W. Numerical Recipes 3rd Edition: The Art of Scientific Computing. New York: Cambridge: 2007. Online: https://books.google.com/books?hl=en&lr=&id=1aAOdzK3FegC&pgis=1

Remouchamps VM, Letts N, Vicini FA, Sharpe MB, Kestin LL, Chen PY, Martinez AA, Wong JW. Initial clinical experience with moderate deep-inspiration breath hold using an active breathing control device in the treatment of patients with left-sided breast cancer using external beam radiation therapy. Int J Radiat Oncol Biol Phys. 2003; 56:704–15. Online: http://www.ncbi.nlm.nih.gov/pubmed/12788176. [PubMed: 12788176]

Rosenzweig KE, Hanley J, Mah D, Mageras G, Hunt M, Toner S, Burman C, Ling CC, Mychalczak B, Fuks Z, Leibel SA. The deep inspiration breath-hold technique in the treatment of inoperable non-small-cell lung cancer. Int J Radiat Oncol Biol Phys. 2000

Seppenwoolde Y, Shirato H, Kitamura K, Shimizu S, Van Herk M, Lebesque JV, Miyasaka K. Precise and real-time measurement of 3D tumor motion in lung due to breathing and heartbeat, measured during radiotherapy. Int J Radiat Oncol Biol Phys. 2002

Seregni M, Paganelli C, Lee D, Greer PB, Baroni G, Keall PJ, Riboldi M. Motion prediction in MRI-guided radiotherapy based on interleaved orthogonal cine-MRI. Phys Med Biol. 2016

Sheng JC, P WR, T AA, J AM, J RB, K Cai J, Read PW, Altes TA, Molloy JA, Brookeman JR, Sheng K. Evaluation of the reproducibility of lung motion probability distribution function (PDF) using dynamic MRI. Phys Med Biol. 2007

Shirato H, Seppenwoolde Y, Kitamura K, Onimura R, Shimizu S. Intrafractional Tumor Motion: Lung and Liver. Semin Radiat Oncol. 2004

Shirato H, Shimizu S, Kitamura K, Nishioka T, Kagei K, Hashimoto S, Aoyama H, Kunieda T, Shinohara N, Dosaka-Akita H, Miyasaka K. Four-dimensional treatment planning and fluoroscopic real-time tumor tracking radiotherapy for moving tumor. Int J Radiat Oncol Biol Phys. 2000

von Siebenthal M, Szekely G, Gamper U, Boesiger P, Lomax A, Cattin P. 4D MR imaging of respiratory organ motion and its variability. Phys Med Biol. 2007a; 52:1547–64. Online: http://www.ncbi.nlm.nih.gov/pubmed/17327648. [PubMed: 17327648]

von Siebenthal M, Székely G, Lomax AJ, Cattin PC. Systematic errors in respiratory gating due to intrafraction deformations of the liver. Med Phys. 2007b

Stemkens B, Tijssen RHN, de Senneville BD, Lagendijk JJW, den Berg van CAT. Image-driven, model-based 3D abdominal motion estimation for MR-guided radiotherapy. Phys Med Biol. 2016

Stevens CW, Munden RF, Forster KM, Kelly JF, Liao Z, Starkschall G, Tucker S, Komaki R. Respiratory-driven lung tumor motion is independent of tumor size, tumor location, and pulmonary function. Int J Radiat Oncol Biol Phys. 2001

Tian Q, Huhns MN. Algorithms for subpixel registration Comput. Vision, Graph Image Process. 1986; 35:220–33.

Tryggestad E, Flammang A, Hales R, Herman J, Lee J, McNutt T, Roland T, Shea SM, Wong J. 4D tumor centroid tracking using orthogonal 2D dynamic MRI: implications for radiotherapy planning. Med Phys. 2013

Verma PS, Wu H, Langer MP, Das IJ, Sandison G. Survey: Real-time tumor motion prediction for image-guided radiation treatment. Comput Sci Eng. 2011

Wong JW, Sharpe MB, Jaffray DA, Kini VR, Robertson JM, Stromberg JS, Martinez AA. The use of active breathing control (ABC) to reduce margin for breathing motion. Int J Radiat Oncol Biol Phys. 1999

Yushkevich PA, Wang H, Pluta J, Avants BB. From label fusion to correspondence fusion: A new approach to unbiased groupwise registration. Proceedings of the IEEE Computer Society Conference on Computer Vision and Pattern Recognition. 2012

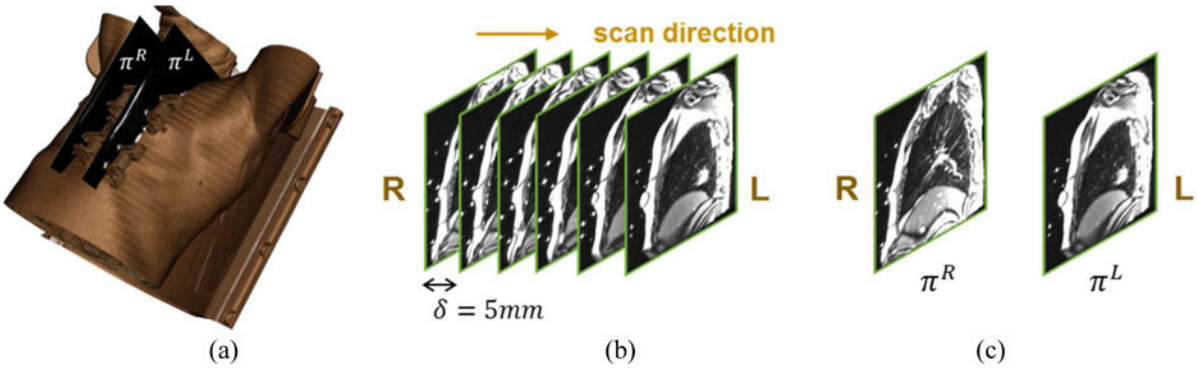

Figure 1.

Image acquisition. (a) Volume rendering of the chest and four fiducials overlaid with two-slice scan planes. (b) Multi-slice 2D images represented from the right to the left. (c) Two-slice scan images at locations $\boldsymbol{\pi}^R$ and $\boldsymbol{\pi}^L$.

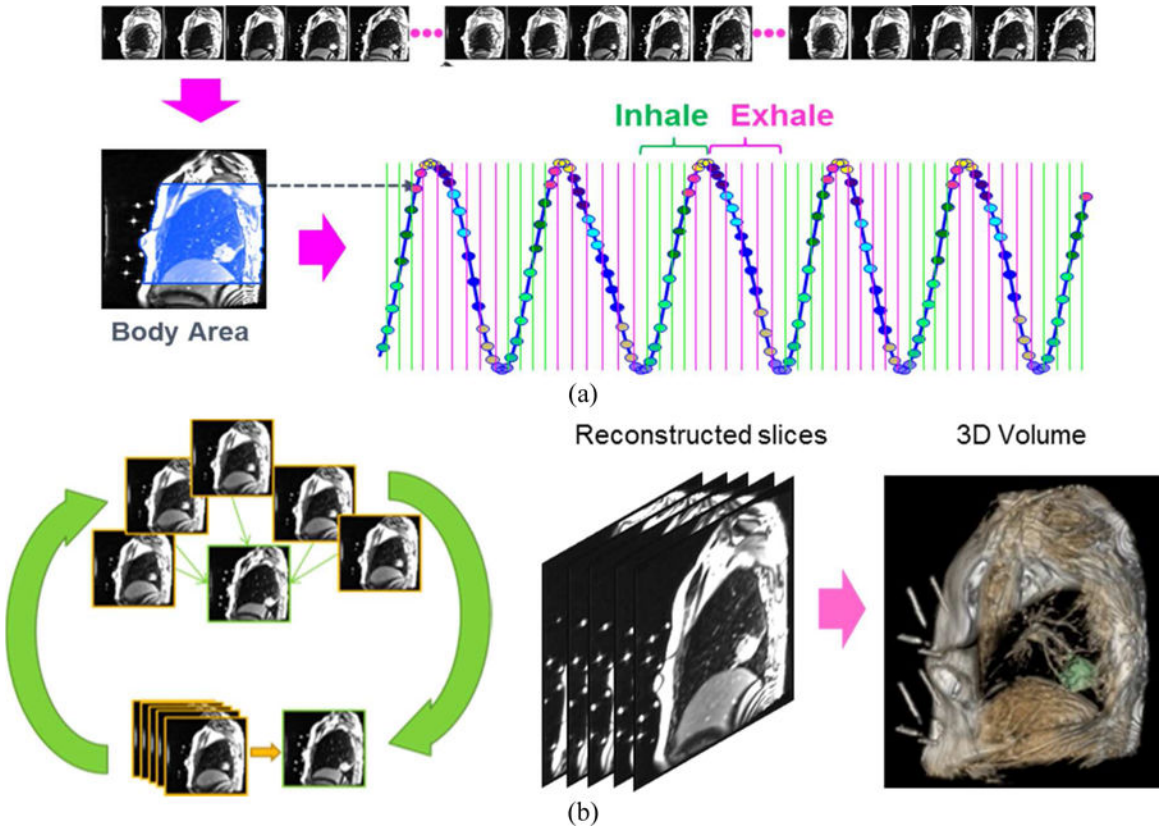

Figure 2.

The 4D-MRI reconstruction process. (a) Phase binning based on body area. The blue region on the left image shows the automatically computed body area including the lung. (b) 4D-MRI reconstruction by groupwise registration. For each breathing phase, each slice image is reconstructed by groupwise registration of multiple sorted images (left). Slice reconstruction is repeated for all slices, and a 3D reconstruction at each breathing phase is computed by stacking the reconstructed slice images (middle). Tumor is then segmented from the reconstructed 4D-MRI to form a tumor template (right, green indicates the segmented tumor).

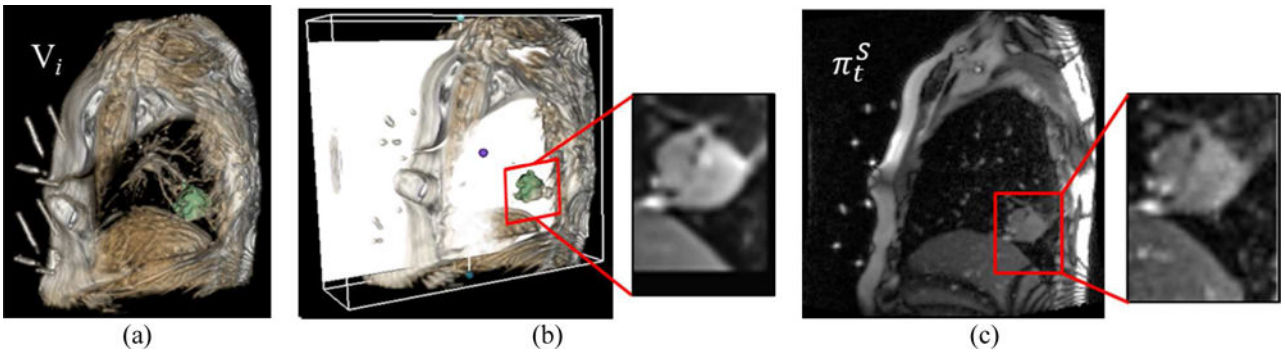

Figure 3.

Tumor tracking by 3D-2D registration. (a) 3D volume, V_i, in the same phase for a particular time point, *t*, of π_t^S. (b) ROI from R_i on the matched plane (white plane) to π_t^S. (c) ROI from π_t^S.

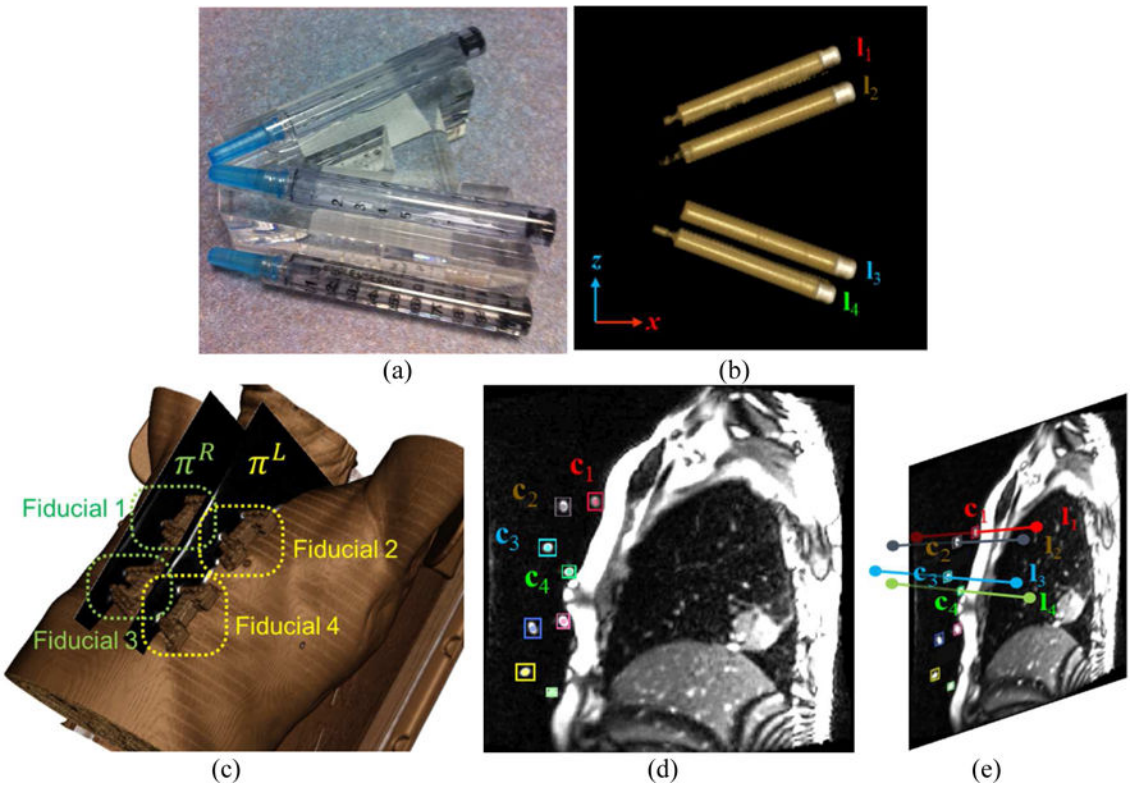

Figure 4.

Fiducial tracking. (a) The photograph of the fiducial, composed of 4 cylinders filled with normal saline. (b) Volume rendering of the fiducial (cylinders only). (c) Locations of four fiducials on volumetric rendering. (d) Fiducial segmentation in 2D MR image (colored boxes). (e) 3D fiducial tracking by matching 3D fiducial model (4 line segments) to the segmented fiducial markers shown in (d).

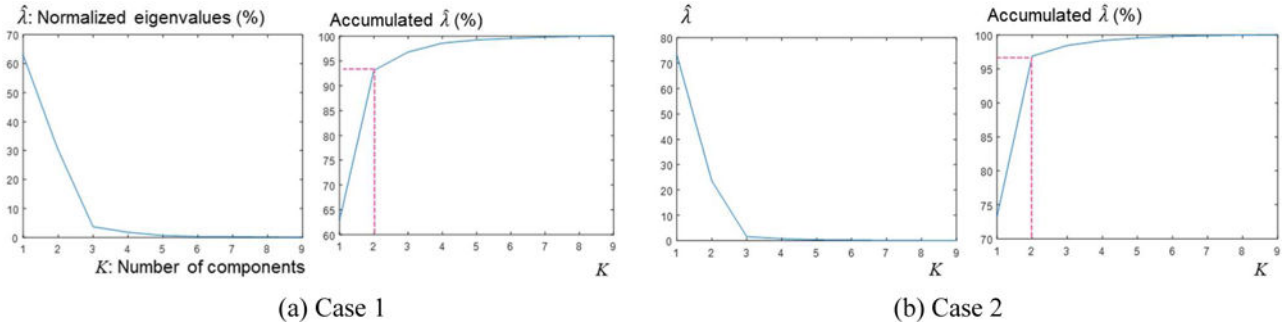

Figure 5.
Plots of normalized percentage eigenvalues of **D**

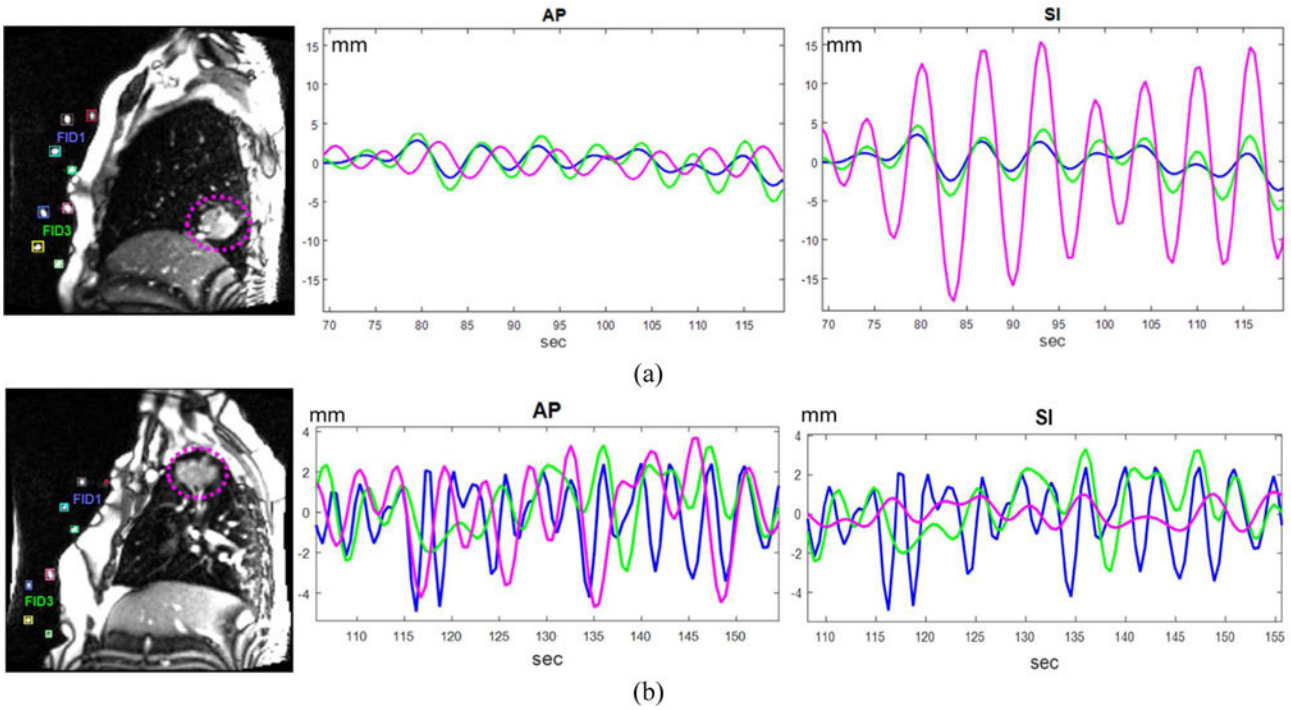

Figure 6.

Tumor motion and surrogate signal estimated from fiducials. The magenta dotted circles in the left images indicate the tumors. The magenta, blue, and green colors in the middle and right images represent the tumor, fiducial 1 and fiducial 3, respectively. (a) The tumor locates at lower lobe of the right lung and shows major motion in the SI direction. (b) The tumor locates at upper lobe of the right lung and shows major motion in the AP direction.

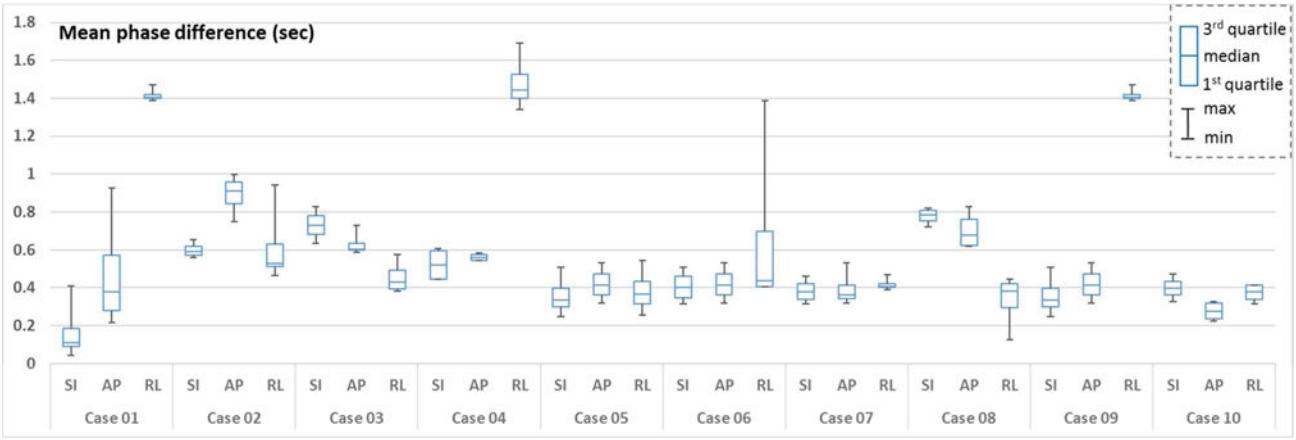

Figure 7.

Box plots of the mean phase differences between four fiducial motions and the tumor motion along each direction - SI: superior-inferior, AP: anterior-posterior, RL: right-left.

Table 1

Tumor tracking accuracy. Mean ± standard deviation (max) in mm. SI: superior-inferior, AP: anterior-posterior, RL: right-left.

Case	SI	AP	RL	3D
1	0.64 ± 0.31	0.97 ± 0.64	1.03 ± 0.75	1.52 ± 1.09 (3.02)
2	1.01 ± 0.51	1.08 ± 0.69	1.12 ± 1.01	1.93 ± 1.21 (3.57)
3	0.57 ± 0.48	0.88 ± 0.75	1.23 ± 0.79	1.56 ± 1.02 (3.31)
4	0.51 ± 0.41	1.02 ± 0.79	1.32 ± 0.87	1.73 ± 1.04 (3.15)
5	0.45 ± 0.39	0.91 ± 0.63	1.03 ± 0.73	1.43 ± 1.21 (2.97)

Table 2

Comparison between the tumor motion signal and fiducial motion signals: cross-correlation and phase differences.

	Tumor location*	Tumor motion	Cross-correlation				Phase difference in seconds (mean ± standard deviation)			
			Fid 1	Fid 2	Fid 3	Fid 4	Fiducial 1	Fiducial 2	Fiducial 3	Fiducial 4
Case 01	RL	SI	36.14	36.14	38.00	36.23	0.043 ± 0.14	0.108 ± 0.21	0.108 ± 0.21	0.409 ± 0.44
		AP	37.92	37.73	37.71	36.65	0.301 ± 0.29	0.215 ± 0.39	0.452 ± 0.47	0.925 ± 0.54
		RL	15.31	16.14	16.73	16.92	1.469 ± 1.10	1.405 ± 1.04	1.405 ± 0.93	1.389 ± 1.03
Case 02	RU	SI	16.52	9.48	16.62	14.42	0.559 ± 0.47	0.655 ± 0.55	0.575 ± 0.52	0.607 ± 0.58
		AP	9.44	9.50	11.59	11.48	0.999 ± 0.74	0.942 ± 0.80	0.747 ± 0.52	0.878 ± 0.81
		RL	9.24	9.43	8.13	9.14	0.527 ± 0.49	0.463 ± 0.60	0.942 ± 0.81	0.527 ± 0.61
Case 03	LU	SI	15.91	22.39	20.14	14.21	0.763 ± 0.72	0.634 ± 0.69	0.699 ± 0.72	0.826 ± 0.79
		AP	12.67	18.48	17.32	15.43	0.603 ± 0.67	0.587 ± 0.56	0.604 ± 0.58	0.731 ± 0.74
		RL	9.32	11.24	11.02	9.21	0.463 ± 0.44	0.383 ± 0.42	0.399 ± 0.45	0.575 ± 0.76
Case 04	RM	SI	11.57	16.81	8.00	7.45	0.447 ± 0.63	0.447 ± 0.48	0.591 ± 0.63	0.607 ± 0.68
		AP	8.82	9.58	9.99	9.02	0.575 ± 0.54	0.543 ± 0.60	0.543 ± 0.60	0.583 ± 0.60
		RL	5.13	4.96	5.22	5.01	1.421 ± 1.07	1.693 ± 0.99	1.341 ± 1.06	1.469 ± 1.11
Case 05	LM	SI	16.31	15.47	15.21	14.04	0.247 ± 0.33	0.314 ± 0.31	0.359 ± 0.43	0.507 ± 0.48
		AP	13.48	14.30	12.96	12.51	0.375 ± 0.42	0.319 ± 0.40	0.451 ± 0.40	0.531 ± 0.52
		RL	7.73	8.16	8.52	9.01	0.543 ± 0.36	0.399 ± 0.32	0.335 ± 0.32	0.255 ± 0.44
Case 06	RU	SI	14.23	16.89	15.76	13.97	0.447 ± 0.33	0.314 ± 0.31	0.359 ± 0.43	0.507 ± 0.48
		AP	11.98	12.09	12.21	10.31	0.375 ± 0.42	0.319 ± 0.40	0.451 ± 0.40	0.531 ± 0.52
		RL	8.43	8.96	9.01	8.89	0.469 ± 1.10	0.405 ± 1.04	0.405 ± 0.93	1.389 ± 1.03
Case 07	LM	SI	13.51	14.96	13.04	13.33	0.347 ± 0.33	0.314 ± 0.31	0.459 ± 0.43	0.407 ± 0.38
		AP	12.13	12.94	12.08	11.29	0.375 ± 0.42	0.319 ± 0.40	0.351 ± 0.40	0.531 ± 0.52
		RL	7.31	7.85	7.99	8.41	0.469 ± 0.30	0.405 ± 0.34	0.405 ± 0.33	0.389 ± 0.23
Case 08	RM	SI	11.98	11.31	11.56	10.39	0.803 ± 0.40	0.821 ± 0.52	0.764 ± 0.52	0.721 ± 0.52
		AP	10.26	9.31	9.88	9.76	0.826 ± 0.46	0.737 ± 0.48	0.617 ± 0.54	0.622 ± 0.58
		RL	6.12	6.89	5.98	6.35	0.413 ± 0.34	0.349 ± 0.26	0.445 ± 0.48	0.127 ± 0.22
Case 09	RU	SI	15.73	11.21	10.57	9.48	0.247 ± 0.33	0.314 ± 0.31	0.359 ± 0.43	0.507 ± 0.48
		AP	9.32	10.36	8.11	7.05	0.375 ± 0.42	0.319 ± 0.40	0.451 ± 0.40	0.531 ± 0.52

	Tumor location*	Tumor motion	Cross-correlation				Phase difference in seconds (mean ± standard deviation)			
			Fid 1	Fid 2	Fid 3	Fid 4	Fiducial 1	Fiducial 2	Fiducial 3	Fiducial 4
Case 10		RL	5.93	6.13	6.18	6.84	1.469 ± 1.10	1.405 ± 1.04	1.405 ± 0.93	1.389 ± 1.03
	LL	SI	20.13	21.14	17.31	15.61	0.373 ± 0.50	0.328 ± 0.54	0.421 ± 0.52	0.473 ± 0.50
		AP	13.21	13.04	12.89	12.56	0.226 ± 0.35	0.237 ± 0.48	0.317 ± 0.54	0.326 ± 0.35
		RL	8.91	9.34	9.41	9.58	0.413 ± 0.34	0.345 ± 0.48	0.315 ± 0.54	0.413 ± 0.34

*Tumor locations - RU: right upper, RM: right middle, RL: right lower, LU: left upper, LM: left middle, LL: left lower.

Table 3

Comparison between tumor motion and ITV for normal breathing scan.

ITV comparison (%)	Case 01	Case 02	Case 03	Case 04	Case 05	Case 06	Case 07	Case 08	Case 09	Case 10
Sensitivity	82.4 ± 10.7	89.1 ± 5.5	88.3 ± 6.4	87.9 ± 8.3	85.6 ± 9.4	85.1 ± 8.9	82.3 ± 7.2	83.5 ± 9.4	85.4 ± 9.3	81.6 ± 5.4
Normal tissue	53.1 ± 6.1	38.2 ± 7.4	39.6 ± 6.3	43.9 ± 8.4	44.2 ± 5.6	43.1 ± 7.1	48.2 ± 6.4	45.4 ± 7.3	43.2 ± 8.1	49.1 ± 5.6